Journal of Physics and Chemistry of Solids 154 (2021) 110061

Contents lists available at ScienceDirect

Journal of Physics and Chemistry of Solids

journal homepage: http://www.elsevier.com/locate/jpcs

Insights into the hydrogen adsorption on deposited graphene oxide by zirconia and gold nanoparticles

Bahareh Feizi Mohazzab [a], Babak Jaleh [a,*], Sadegh Khazalpour [b], Mahmoud Nasrollahzadeh [c], Masoud Zare [d], Ho Won Jang [e], Mohammadreza Shokouhimehr [e]

[a] Department of Physics, Faculty of Science, Bu-Ali Sina University, Hamedan, 65174, Iran
[b] Faculty of Chemistry, Bu-Ali Sina University, 65174, Hamedan, Iran
[c] Department of Chemistry, Faculty of Science, University of Qom, Qom, 3716146611, Iran
[d] Department of Catalyst, Research Institute of Petroleum Industry (RIPI), Tehran, Iran
[e] Department of Materials Science and Engineering, Research Institute of Advanced Materials, Seoul National University, Seoul, 08826, Republic of Korea

ARTICLE INFO

Keywords:
Graphene oxide
Zirconia
Au NPs
Laser ablation in liquid (LAL)
Hydrogen storage

ABSTRACT

Here, to investigate the hydrogen storage capacity by carbonaceous compounds, graphene oxide (GO) was utilized. To evaluate the influence of metal oxide, GO was modified by zirconium oxide (ZrO_2) through the refluxing method (GO-ZrO_2). Laser ablation in liquid (LAL) was deployed to fabricate gold nanoparticles (Au NPs), which were then deposited on GO-ZrO_2 (GO-ZrO_2/Au) to assess the effect of metal NPs on hydrogen adsorption performance. Different analyses characterized the synthesized nanocomposites and the results suggest the successful immobilization of ZrO_2 and Au NPs. The nanocomposites were deposited on a stainless steel mesh by electrophoretic deposition (EPD) and used in the electrochemical cell as working electrodes. Hydrogen storage capacity was assessed by electrochemical route in an alkaline medium under ambient conditions. The comparison of cyclic voltammetry (CV) revealed that increasing hydrogen charge is the courtesy of ZrO_2 and Au NPs. The maximum hydrogen charge achieved by GO-ZrO_2/Au was about 180 Cg^{-1}. The best electrode stability was assessed and the results indicated that EPD was such an effective method that the electrode offered good stability under prolonged analysis. The results suggest that the synthesized nanocomposites can be considered as potent candidates in hydrogen production and storage.

1. Introduction

In the present century, there is quite an extensive diversity of hazards involved with growing energy consumption along with increasing population and improving industrialization [1]. Of course, there are potential risks regarding carbon footprint, greenhouse gases, and global warming. The underlying fact is that fossil fuels cause irreversible damages to the environment and their shortage must be considered a major problem. The drawbacks of fossil fuels can be avoided by the application of alternative biofriendly energy resources. Having increased demand for fuels, research is focused on the design and development of power source devices. To fulfill such targets, the main aspect of efforts is producing energy *via* greener pathways as well as energy storage through cost-effective devices for widespread utilization [2]. Producing hydrogen from water is attractive because, in contrast to fossil fuel, hydrogen is renewable and bio-friendly, as well as it omits greenhouse gases [3]. The produced hydrogen can be stored in liquid, gas, and solid state forms. In fact, high pressure compression and liquefaction are the most impractical processes for hydrogen storage in liquid and gas phases [4], respectively which changes the attention to hydrogen storage by physisorption process in nanostructured materials such as carbonaceous and metal organic framework (MOF) [4,5]. Based on physisorption, hydrogen spillover mechanism by carbon materials [6], zeolites [7], and MOF [8,9] has been extensively reported in literature. In the spillover process, hydrogen dissociation source, receptor and connection are critical factors [10]. Highly distributed metals (hydrogen dissociation source) increase the metal surface area and provide an adequate connection between metal and carbon receptors [10]. It is worth mentioning that the metal NPs overloading adversely affected; the optimized loading was achieved when the surface of the receptor is mainly accessible [11–14]. An excellent receptor provides more host sites for hydrogen adsorption; modification of surface

* Corresponding author.
E-mail address: jaleh@basu.ac.ir (B. Jaleh).

https://doi.org/10.1016/j.jpcs.2021.110061
Received 29 November 2020; Received in revised form 8 March 2021; Accepted 16 March 2021
Available online 20 March 2021

chemistry (doping of receptor by boron, nitrogen) was suggested for improving the surface area. Comparing adding oxygen functional groups documented that surface oxygen groups stabilize the hydrogen and offer bridges [15–17], as a consequence hydrogen atoms can diffuse to the host sites of the receptor, which were inaccessible before [17,18]. In addition, oxygen containing functional groups such as hydroxyl groups increase hydrophilicity offering the most effective property for the interaction between the surface of materials and liquid [19]. The last but not the least factor has been investigated to fulfill intimate contact. The physical loading of metals or metal oxides on carbon receptors has been suggested as the easiest approach to overcome the lack of bridges between the hydrogen dissociation source and receptor [11,20,21].

Graphene oxide (GO), which has a large surface area and different functional groups, is a good candidate as a substrate in various research fields; for instance, catalytic activity [22,23] and energy storage [24–26]. An overview of the literature indicates that different components have modified GO as hydrogen storage substrate [27–36]. GO surface offers a good space for hydrogen adsorption, diffusion and storage. In addition, oxygen-containing functional groups such as hydroxyl groups accelerate the adsorption of hydrogen on carbon surface materials [37]. Increasing hydrogen storage capacity was achieved by modifying surface oxygen groups; for example, adding transition metals [38,39] and metal oxides such as TiO_2, ZnO, and ZrO_2 [40–43] is the most convenient method to improve the surface area and electrochemical performance [44]. Having unique mechanical, thermal, and structural properties, zirconia (ZrO_2) has been utilized in a diverse range of fields [45]. Metal NPs have been exceedingly utilized as adsorbent species in hydrogen storage [1,26,39,46–51]. The decoration of substrates with NPs effectively promotes applications, which are unattainable by substrate individually. Considering the specific properties of Au NPs, they have been used as improving agents in hydrogen production [46] and analytical sensitivity [52]. Different approaches to decorate substrates with Au NPs have been reported in the literature such as chemical deposition [53], seed-mediated growth [54] and laser ablation in liquid (LAL) [23,55]; the last one has attracted attention because of its adjustable parameters and eliminating of contaminating reagents [56]. Furthermore, LAL is a physical method to generate NPs by different shapes and morphology [57]. Although production NPs in gram scale is already accessible, there are some ways to eradicate the boundaries for the scaling-up of the production without a reduction in the quality of NPs colloidal [58]. In the quest for a suitable method tighter focusing, extending ablation time, and increasing laser energy have been recommended. It is worth mentioning that the aforementioned methods need to optimized parameters that not only do not prevent reaching the whole energy of laser pulse to target, but also offer a high production rate [59]. High-repetition-rate and high power laser was applied as an easy setup for gram scale production about 4 g/h [60]. The results suggested that laser-induced bubbles were elapsed because of high scanning speed, and the laser beam can effectively reach to the surface of target. A high-power nanosecond laser and ultrasonication were utilized to synthesize organic NPs; indeed, ultrasonication led to restrict aggregation, which increases production rate and efficiency [61]. Furthermore, the thickness of liquid which covers target surface was recommended as one of the crucial parameter [58,62].

Among deposition methods, electrophoretic deposition (EPD) has been extensively used down to its adjustable parameters and deposition quality. EPD has been considered an effective method for the deposition of nanocomposites on conductive substrates [63]. These deposited substrates have the potential to employ in different areas such as oil-water separation [64] and ethanol electro-oxidation [65]. Electrochemical hydrogen storage through cyclic voltammetry (CV) is a prevailing method to study adsorption/desorption of hydrogen in detail [1]. Water decomposition takes place in a cathodic direction; consequently, hydrogen is produced from water. Hydrogen atoms are migrated to the surface of the electrodes under the applied potential and are desorbed in an anodic sweep [1].

Considering consensus regarding environmentally friendly methods leads us to introduce a new nanocomposite close to this target using GO as a substrate. To investigate the effect of the oxygen-containing functional group on hydrogen storage, zirconia NPs were physically loaded on GO surfaces *via* the reflux route. Nanocomposites decorated with Au NPs were accomplished by LAL method to prove Au NPs influence on hydrogen adsorption performance. Nanocomposites were deposited on stainless steel mesh, a conductive substrate, by the EPD method and used as working electrodes. The CV was deployed to assess hydrogen storage on a working electrode in an alkaline medium.

2. Methods

2.1. Instruments and reagents

All chemical materials were purchased from Merck Chemical Co. with high purity. The ZrO_2 NPs were purchased from Asiapajohesh Company and used as received. The stainless steel mesh (200 mesh) was used as the conductor substrate and a Fiber laser (RFL-P30Q, $\lambda = 1064$ nm and 30W) was applied on a piece of high purity gold to synthesize Au NPs in deionized water at ambient temperature. The characterization of nanocomposites was performed by X-ray diffraction (XRD, D8-Advance Bruker) in the 2θ range of 10–80° at the wavelength of 0.154 nm. Applying Fourier transform infrared (FT-IR, Thermo Nicolet) is useful to investigate the nature of nanocomposite. To measure the elemental composition of the nanocomposites, X-ray photoelectron spectroscopy (XPS) was deployed; all the binding energy being adjusted through the C1s peak located at 284 eV. The changes of the pore size and surface area of the nanocomposites were illustrated by Brunauer-Emmett-Teller (BET, BELSORP-mini II) and Barret-Joyner-Halenda (BJH) analyses, respectively. Morphology was surveyed by scanning electron microscopy (SEM, TESCAN-MIRA3-XMU) coupled with an energy-dispersive X-ray spectrometry (EDX) system to study the presence of elements. Transmission electron microscopy (TEM, JEM-2100F JEOL and CM120, Netherland) and high resolution electron microscopy (HRTEM, JEM-F200, JEOL Ltd., Japan) were deployed to visualize the morphology of the nanocomposites. Meanwhile, elemental mapping (MAP) represented the distribution of the elements. To elucidate hydrogen production, adsorption and desorption, an Autolab (PSTAT204) instrument was utilized in the potential range of −1.5 to 0.6 in a three conventional cell.

2.2. Synthesis of GO-ZrO_2 nanocomposite

In this work, GO was prepared through graphite oxidation by Hummers' method [66]. To synthesize GO-ZrO_2 nanocomposite, 0.8 g of GO and 0.2 g of commercial ZrO_2 were dispersed separately in 50 mL of deionized water and sonicated for 15 min to reach a homogenous suspension. Subsequently, the ZrO_2 suspension was added to GO suspension and the GO-ZrO_2 nanocomposite was prepared using the refluxing method for 24 h at 100 °C. The final powder was filtered and dried at room temperature.

2.3. Synthesis of GO-ZrO_2/Au NPs nanocomposite

Au NPs were prepared using LAL by a reported method [23]. Briefly, the gold target was placed at the bottom of a cell filled with deionized water such that 2 mm of water covered the whole surface of the target. As LAL was performed, the color of water turned to purple, confirming the fabrication of Au NPs. To prevent agglomeration and absorption of the laser beam by NPs, LAL was performed in 6 stages, each stage taking 5 min. After 5 min, the colloidal product was extracted and LAL was continued with fresh water until 0.01 g of Au NPs was acquired. Afterwards, 0.1 g of GO-ZrO_2 was added to the colloidal Au NPs and the mixture obtained was stirred for 24 h. The final powder was extracted and dried at room temperature. The whole process is depicted in Fig. 1a.

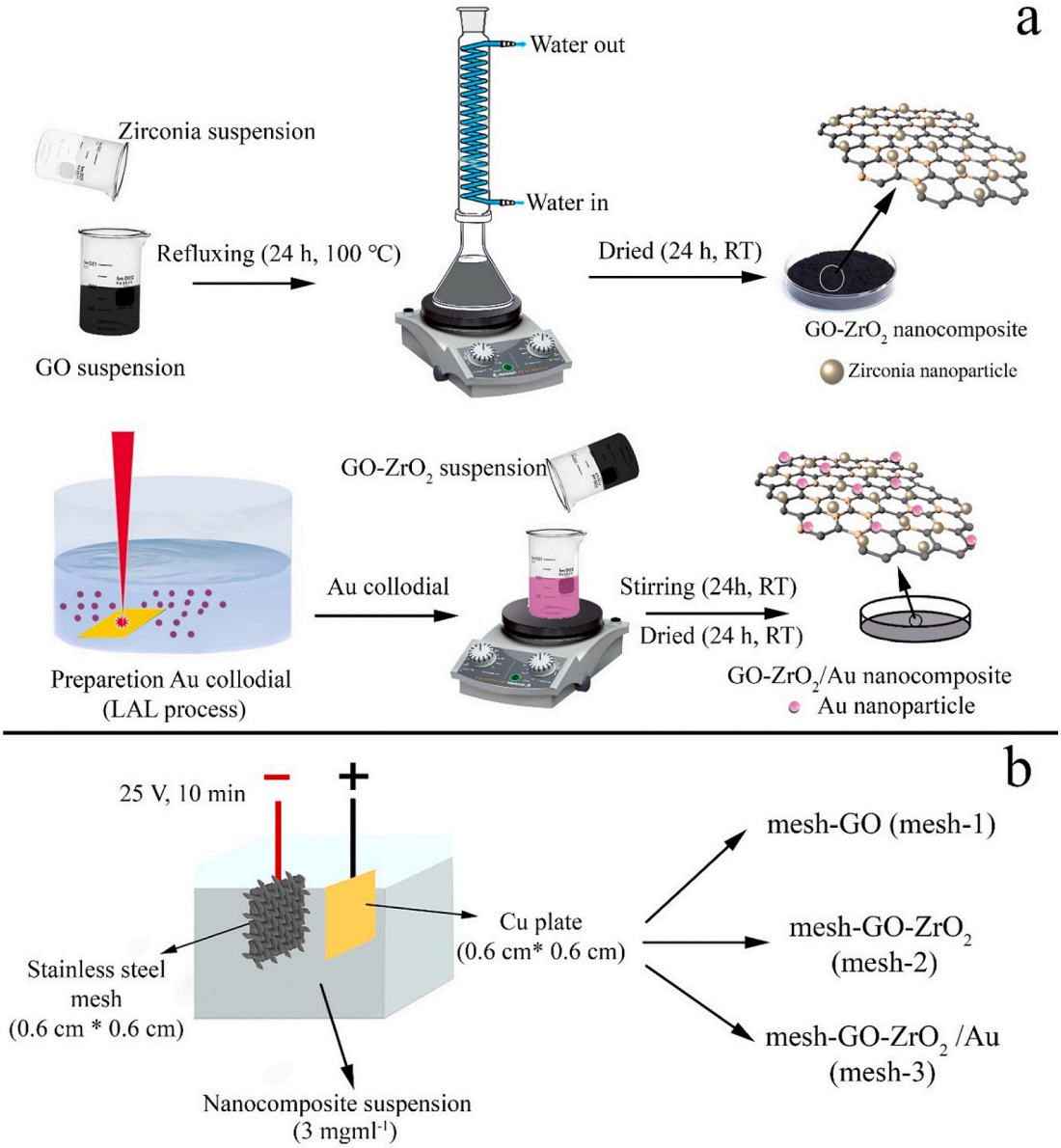

Fig. 1. Schematic of (a) nanocomposites preparation procedure and (b) EPD process for deposition stainless steel mesh.

2.4. Preparation of mesh nanocomposite coating

A stainless steel mesh (0.6 cm × 0.6 cm) washed with acetone and deionized water was used as a substrate. The nanocomposite coating was carried out by the EPD route as follows. A homogenous suspension of the nanocomposites with a concentration of 3 mg mL^{-1} was prepared by adding 0.12 g of the nanocomposites in 40 ml of distilled water and diffused for 1 h at room temperature. The mesh and a piece of copper, vertically faced by 10 mm separation and connected with a DC power source, acted as the anode and cathode, respectively. The EPD parameters were selected as 3 mg ml^{-1}, 25 V and 10 min for nanocomposite concentration, DC voltage and deposition time, respectively. The mesh coated samples were dried at room temperature overnight and named mesh-1, mesh-2 and mesh-3, representing mesh-GO, mesh-GO-ZrO_2 and mesh-GO-ZrO_2/Au coating, respectively. The EPD process is schematically shown in Fig. 1b.

2.5. Hydrogen storage measurements

Hydrogen storage measurements were performed by electrochemical setup, a promising method to investigate hydrogen adsorption/desorption. The investigation of electrochemical hydrogen storage was performed using an Autolab (PSTAT204). Pt plate and Ag/AgCl acted as the counter and reference electrodes, respectively, in 1 M KOH as the electrolyte. All the electrochemical measurements were performed in the potential window of −1.5-0.6 at a sweep scan rate of 100 mV/s.

2.6. Nanocomposite characteristic

To estimate the diameter of ZrO_2 NPs, TEM analysis was deployed, Fig. 2, and the mean diameter of NPs was measured by Image J software over 30 NPs. The results suggest that ZrO_2 NPs are almost spherical with the average diameter of 35 nm.

XRD analysis was deployed to investigate the structural properties of the resultant nanocomposites. The XRD patterns of GO-ZrO_2 and GO-ZrO_2/Au are presented in Fig. 3. The sharp peaks suggest that the samples are stabilized in the crystal structure. The broad peak in the range of $2\theta = 20–30^\circ$ corresponds to rGO [67], confirming that GO has been almost reduced during the synthesis of the nanocomposite. The XRD pattern of GO-ZrO_2 exhibits some sharp peaks at $2\theta = 28.17^\circ$,

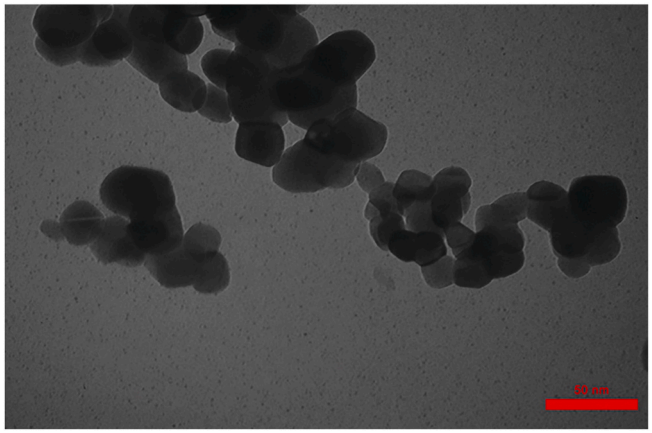

Fig. 2. TEM image of ZrO_2 NPs.

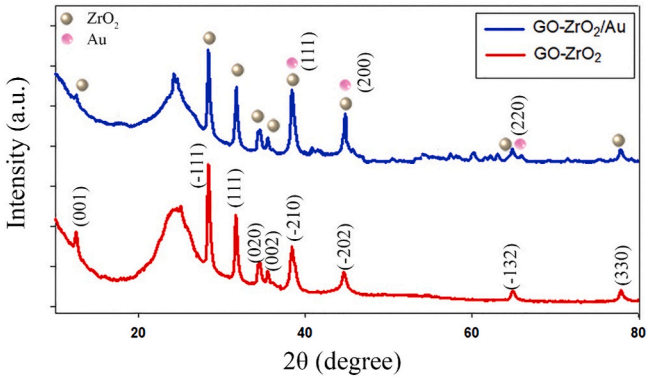

Fig. 3. XRD pattern of GO-ZrO_2 (red line) and GO-ZrO_2/Au (blue line).

31.46°, 34.38°, 38.39°, 45.54°, and four less intensive peaks located at $2\theta = 17.4°$, 35.30°, 65.88° and 77.39°, which are attributed to ZrO_2 NPs planes depicted in Fig. 3 (JCPDS 37-1484). It worth mentioning ZrO_2 has appeared in the monoclinic phase. In addition to ZrO_2 peaks, the XRD pattern of GO-ZrO_2/Au presents three peaks due to Au NPs. The peaks around $2\theta = 38.18°$, 44.39° and 64.57°, derived from planes of the Au (JCPDS 04-0784) [68] are shown in Fig. 3. These strong peaks provide strong evidence for the successful synthesis.

To investigate how Au loading affects nanocomposite structure, the grain size was estimated individually for each peak, listed in Table 1, and the average was calculated. The grain size was estimated using the following equation (Scherrer's low [69]):

$$D = \frac{0.9\lambda}{\beta cos\theta} \quad (1)$$

where $\lambda = 0.154\ nm$ is the wavelength of the X-ray instrument, the full width of half maximum intensity (FWHM) in radian is exhibited by β, and θ is the Bragg diffraction peak. As observed, the grain size of the nanocomposites was increased slightly for each diffraction peak, which is explained by the narrow peaks after immobilization of Au NPs because the only β is different for nanocomposites under the same conditions.

Table 1
Grain size (nm) of GO-ZrO_2 and GO-ZrO_2/Au.

(*hkl*)	GO-ZrO_2	GO-ZrO_2/Au
(-111)	44.70	45.40
(111)	51.33	51.28
(-210)	46.12	58.69
(-202)	29.95	33.47

The average grain size was calculated as about 43.04 and 47.02 nm for GO-ZrO_2 and GO-ZrO_2/Au, respectively. Although TEM analysis shows the average diameter of ZrO_2 was about 35 nm, agglomeration led to changes in the structure of NPs; consequently, the crystallite size was increased [70].

To study the chemical composition of the samples, FTIR analysis was deployed and results are presented in Fig. 4. The hydroxyl groups are important groups for adsorbing hydrogen (Fig. 4a). In Fig. 4b, the absorption peak in the range of 3200–3600 cm^{-1} is attributed to the stretching vibration of –OH groups probably due to the residual water molecule from the synthesis process [71,72]. Furthermore, there is a weak band around the 1600 cm^{-1} due to the vibration of H_2O molecules physically adsorbed on the surface of ZrO_2 [71–74]. The peaks in the range of 400–700 cm^{-1} show Zr-O bonding in ZrO_2 NPs and indicate the monoclinic structure of the ZrO_2 NPs [71], which are corroborated with XRD data. Fig. 4c displays the FTIR spectrum of GO-ZrO_2. Due to coordination between Zr and O on the surface of ZrO_2, the characteristic peak of C=O stretching was shifted from 1650 to 1700 cm^{-1}, and a significant decrease of the intensity was observed [67]. The comparison of the FTIR spectra of GO-ZrO_2 and GO-ZrO_2/Au, Fig. 4c and d, shows no changes after the deposition of Au NPs, which is a clear indication for the physical addition of NPs.

The elemental composition of GO-ZrO_2/Au was investigated by XPS measurement and results are represented in Fig. 5. The wide spectrum, Fig. 5a, shows the presence of ZrO_2 and Au on the surface of GO due to

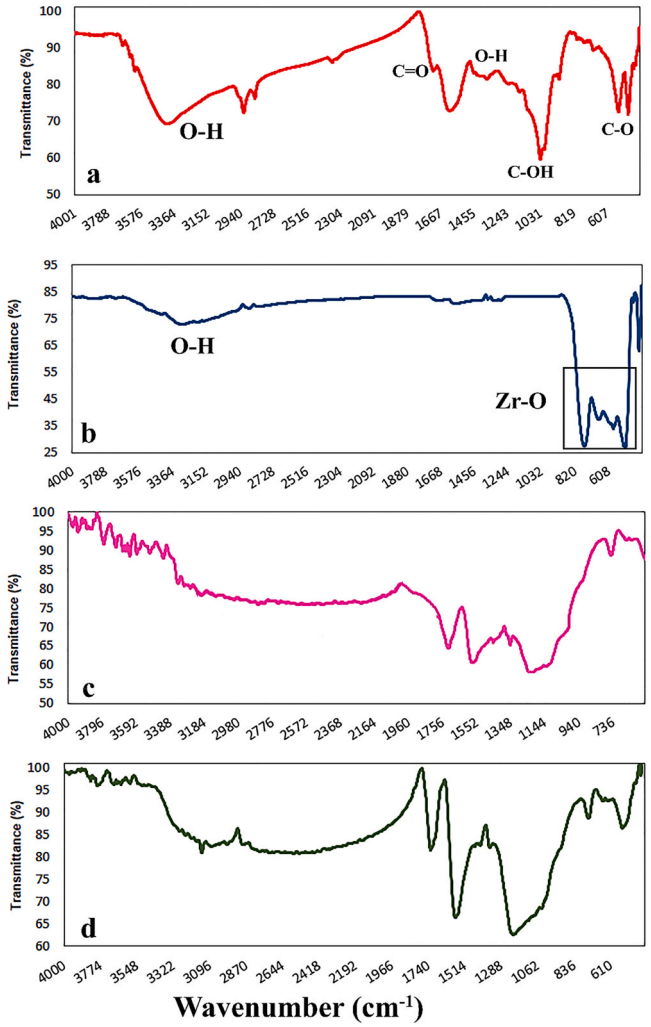

Fig. 4. FTIR spectrum of (a) GO, (b) ZrO_2 NPs, (c) GO-ZrO_2 and (d) GO-ZrO_2/Au.

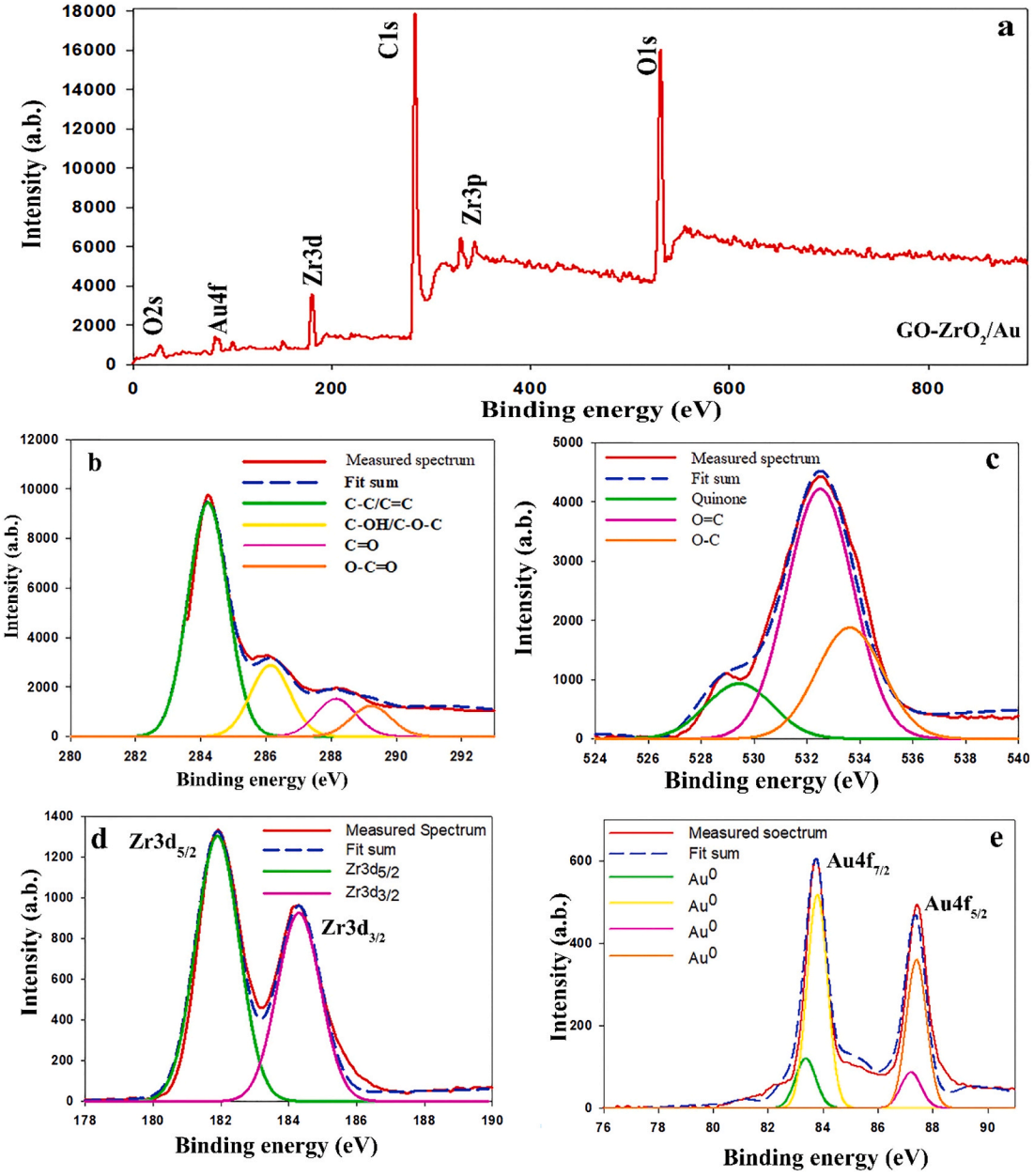

Fig. 5. The XPS analysis of GO-ZrO_2/Au (a) wide spectrum, (b) C1s, (c) O1s, (d) Zr3d and (e) Au4f.

Zr3d, O1s and Au4f characteristic peaks. According to Fig. 5b, the C1s peak located at 284 eV was deconvoluted to four peaks as follows: C-C (286.4 eV), hydroxyl and epoxy group (C-OH/C-O-C, 286.7 eV), carbonyl group (C=O, 288.7 eV) and a carboxyl group (O-C=O, 289 eV), which are signals for the presence of GO sheet [67,75,76]. Three peaks designated to Quinone groups (530 eV), O=C (531.8 eV) and O-C (532.8 eV) are shown in the spectra of O1s [77], Fig. 5c. The $Zr3d_{5/2}$ and $Zr3d_{3/2}$ present at 183.5 eV and 185.5 eV, respectively, confirm the successful immobilization of ZrO_2 NPs. As shown in Fig. 5d, the characteristic peaks of Au4f were deconvoluted to two peaks located at 83.7 eV, attributed to $Au4f_{7/2}$, and 87.6 eV ascribed to $Au4f_{5/2}$ [78]; both peaks indicating the presence of Au NPs in the metal state [79].

The surface characterization of the samples was gauged by nitrogen physisorption at 77 K, adsorption/desorption isotherm and pore size distribution of GO, GO-ZrO_2 and GO-ZrO_2/Au, which were depicted in Fig. 6 and Table 2. Fig. 6a displays the N_2 adsorption/desorption isotherms of the samples, the H_2 hysteresis loop [80] and isotherm type of IV revealed from data in the range from 0.4 to 0.9 compared to relative pressure [81], which is associated to bottleneck pores [82]; as well as a considerable storing nitrogen into pores was declared by comparison isotherms after loading Au NPs. Fig. 6b shows pore distribution of samples through BJH analysis, the major peak of GO, GO-ZrO_2 and GO-ZrO_2/Au is around 2.7 nm, 4.02 nm, 3.08 nm, respectively; indicating the mesoporous structure [83]. As can be seen, the surface area was risen after loading ZrO_2 NPs on the surface of GO; this phenomenon was probably due to the agglomeration of ZrO_2 NPs [84]. The addition of NPs on the surface of GO-ZrO_2 contributes to increases the surface area, which favors hydrogen storage capacity. The comparison of the pore volume of the samples shows a significant increase, affirmed doping NPs has created new pores [85]. Moreover, the average mean diameter was calculated and the results suggest that decreasing pore diameter occurred by adding ZrO_2 NPs, probably down to filling pores.

On the other hand, loading Au NPs increases the average diameter, which is probably due to the immobilization effect and generation of a new porous structure [1,84,86]. It has been reported that increasing the surface area and pore diameter is beneficial for catalytic performance

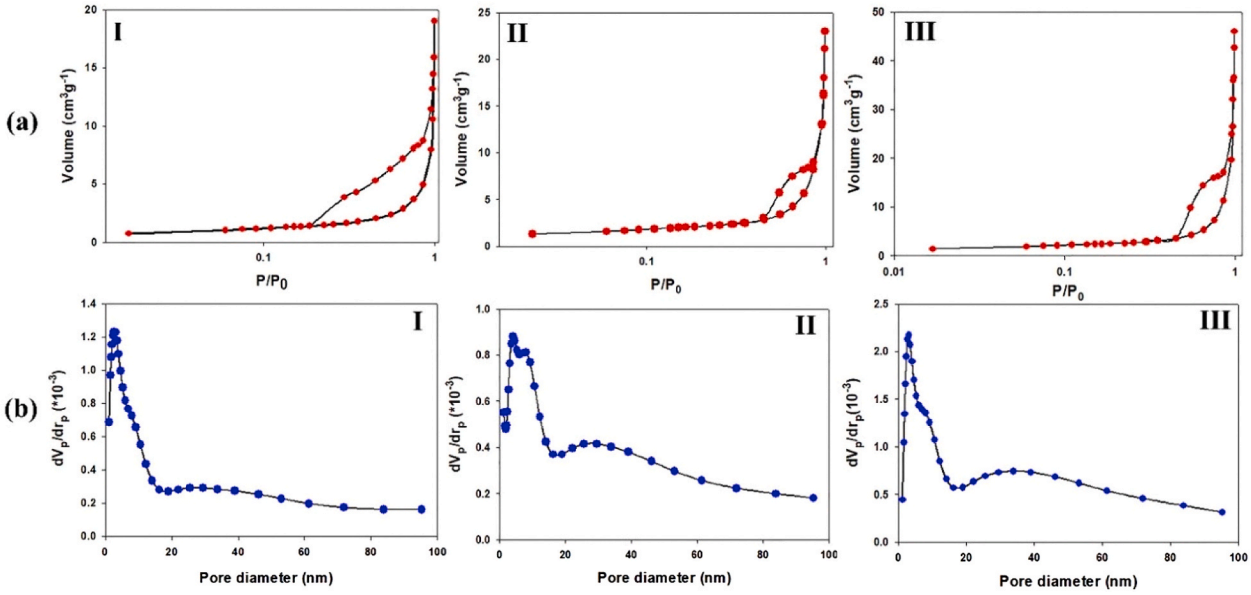

Fig. 6. Nitrogen adsorption/desorption profile (a) and pore diameter distribution (b) of GO (I), GO-ZrO_2 (II) and GO-ZrO_2/Au (III).

Table 2
Surface characterization calculation of GO, GO-ZrO_2 and GO-ZrO_2/Au by nitrogen physisorption at 77 K.

Sample name	BET surface area (m^2g^{-1})	Total pore volume (cm^3g^{-1})	Mean pore diameter (nm)
GO	5.15	0.028	22.00
GO-ZrO_2	7.49	0.035	18.80
GO-ZrO_2/Au	8.79	0.064	29.21

and hydrogen storage. Consequently, it is envisaged that such a high surface area and pore volume as well as wrinkles morphology because of GO lead to increase hydrogen charge capacity [87].

To assess the morphology of samples, the SEM analysis was conducted and the images are presented in Fig. 7. The ocean-like and wrinkle structure of GO offers a good space for loading ZrO_2 NPs and most of which are irregularly decorated cauliflower-like on the surface of GO. As observed in Fig. 7b, in some regions, the agglomeration of ZrO_2 NPs has occurred. As others have claimed, the agglomeration of NPs leads to increased surface area [85,86], which was affirmed by BET

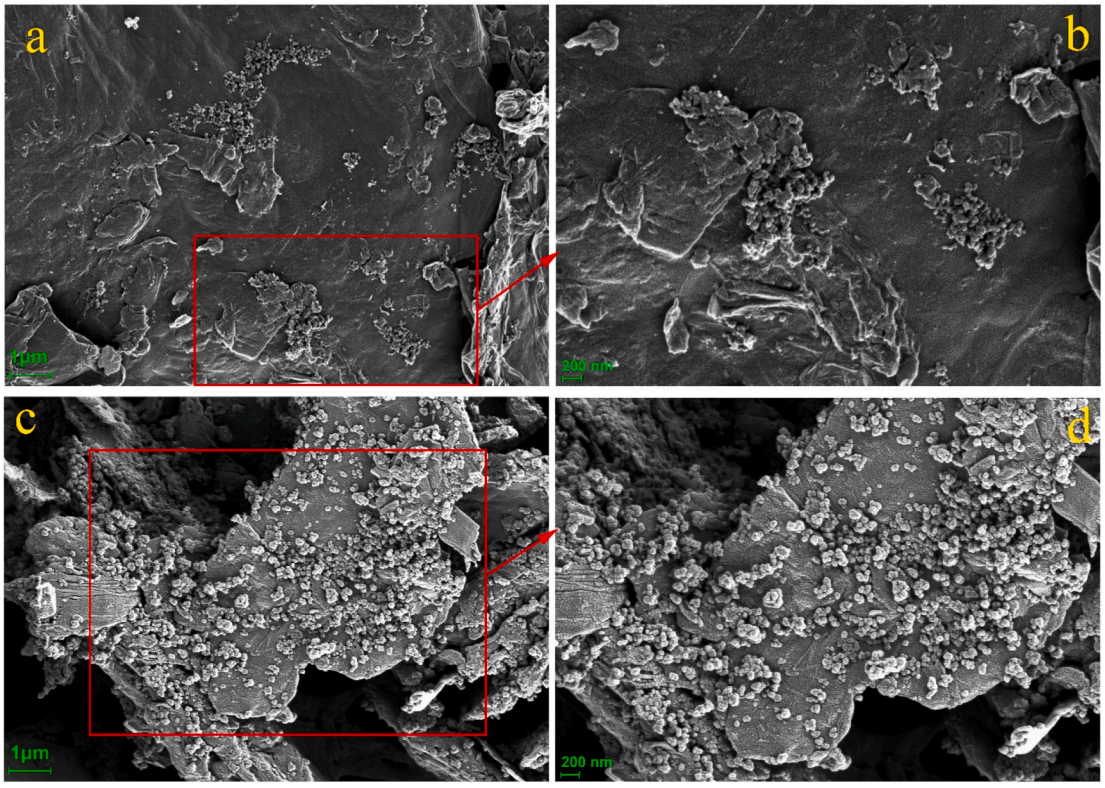

Fig. 7. The SEM images of GO-ZrO_2 (a and b) and GO-ZrO_2/Au (c and d) with different magnifications.

results. The morphology of the GO-ZrO_2 nanocomposite was not changed after immobilization Au NPs, most of which were formed in spherical shape on the surface of GO sheet, see Fig. 7c and d. Loading metal NPs increased the surface area simultaneous with pore volume, which are crucial factors in hydrogen storage [88]. Consequently, improving storage performance was predicted.

TEM analysis can be deployed as a supplement for SEM to distinguish ZrO_2 and Au NPs on the surface of the nanocomposite. The TEM images of GO-ZrO_2 and GO-ZrO_2/Au are shown in Fig. 8. The dark gray sheet presents GO surface; wrinkle morphology was supported by SEM analysis results. Besides, the black region shows that ZrO_2 NPs are aggregated on the surface of GO. Compared with GO-ZrO_2, in Fig. 8b, along with the black region, some black circle is ascribed to Au NPs loading. The comparison of Fig. 8 a and b indicates that some black regions shown by red line in Fig. 8a are probably due to the overlapping or folding of the GO sheets [89]. To clarify the morphological structure of the prepared nanocomposite, HRTEM analysis was conducted and the result of GO-ZrO_2/Au is depicted in Fig. 8c and d. Given that the atomic number of Au is more than that of Zr, the darker regions are due to Au [90]. As it can be observed, the lattice fringes are clear in Fig. 8d. The interplanar spacing is calculated as 3.21 Å, which is consistent with d_{-111} of monoclinic ZrO_2 (JCPDS 37-1484) [91,92] and 2.35 Å from (111) corresponding to the face centered cubic (FCC) structure of Au(JCPDS 04-0784) [68]. Furthermore, the comparison of TEM and HRTEM shows some of the ZrO_2 NPs are accumulated. As a result, the size of ZrO_2 NPs seems larger. The yellow and green rectangles in Fig. 8 a and c show aggregation areas, respectively.

To scrutinize presence and distribution of the elements, EDX and elemental mapping were deployed for nanocomposites, respectively, and depicted in Fig. 9. As observed, EDX analysis illustrates the presence of Zr and Au on the surface of samples, confirming the successful loading of NPs on the surface of GO by the physical stirring method, and the uniform deposition is clearly observed by elemental mapping.

2.7. Electrochemical measurement

2.7.1. Cyclic voltammetry details

CV is a reliable method to investigate the adsorption/desorption of hydrogen by the working electrode. If the electrode potential is lower than water decomposition potential, hydrogen can be produced from water and adsorbed on the host active site of the working electrode [93] through the following reactions (cathodic direction):

$$H_2O + e^- \rightarrow H + OH^- \quad (2)$$

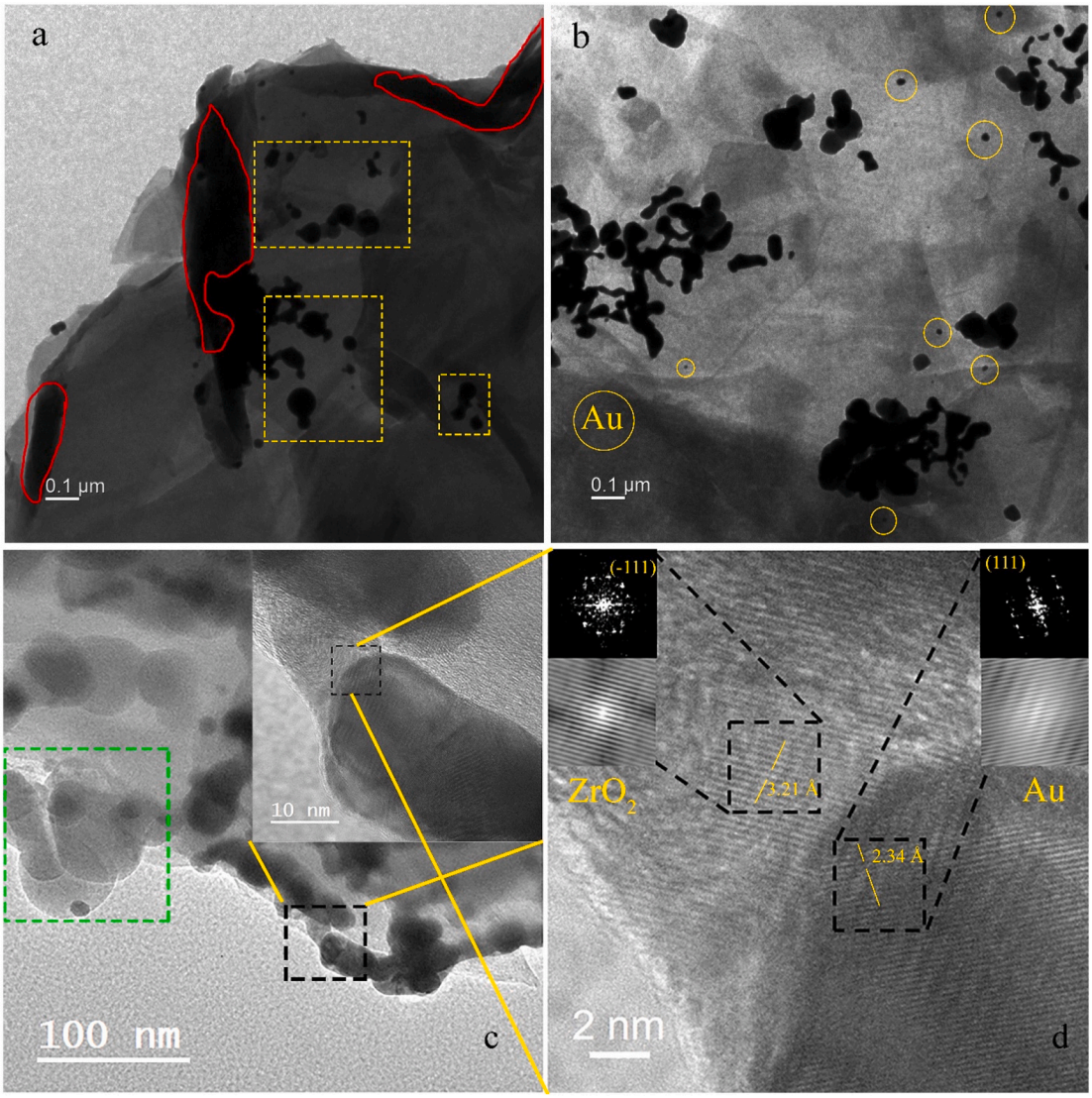

Fig. 8. TEM illustration of (a) GO-ZrO_2 and (b) GO-ZrO_2/Au, (c and d) HRTEM images of GO-ZrO_2/Au with different magnification; inset picture in panel c shows an enlarged view of the black dotted rectangle, and inset pictures in panel d represent lattice fringe.

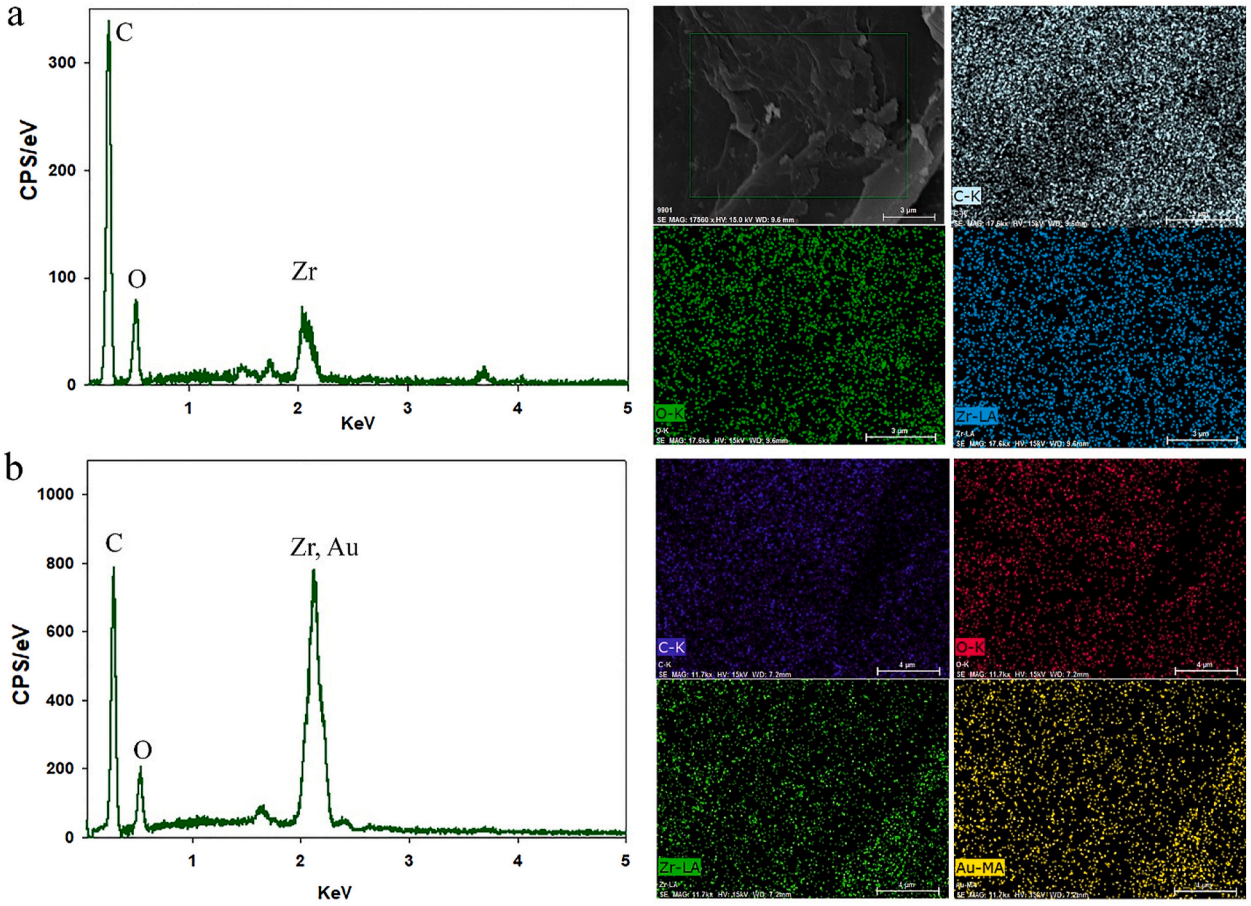

Fig. 9. The EDX and elemental mapping of (a) GO-ZrO_2 and (b) GO-ZrO_2/Au.

$$<W> + xH \rightarrow <WH>_x \quad (3)$$

where <W> represents a host active site on the working electrode surface. The adsorbed hydrogen on the surface of the working electrode was released in the anodic direction [1]. The total reaction was taken place as follow:

$$< W > \ + xH_2O \ + \ xe^- \rightleftarrows < WH > x \ + \ xOH^- \quad (4)$$

The anodic peak area reveals the amount of hydrogen desorbed from the surface of the working electrode [1,40,94]. A baseline was designated to separate the double layer and anodic peak regions; indeed, the baseline is a gauge to introduce faradaic region where hydrogen atoms are being segregated. The following equation was used for hydrogen desorption measurement:

$$Q_H = \frac{1}{\vartheta} \int_{v_i}^{v_f} (I_a - I_{dl}) dE \quad (5)$$

where ϑ is the sweep rate, v_i and v_f are the initial and final potentials of the anodic peak, dE is the potential window, and the anodic peak and double layer charging current are labeled as I_a and I_{dl}, respectively. It must be pointed out that all the parameters are chosen by the CV data from each cycle.

2.8. Hydrogen storage investigation

Hydrogen adsorption/desorption was evaluated and compared in a 1 M KOH electrolyte solution with a three-electrode configuration at a sweep rate of 100 mVs^{-1}. All the samples, deposited on stainless steel mesh, were used as the working electrodes while a Pt plate and Ag/AgCl served as the counter and the reference electrodes, respectively. The CV curves of the mesh substrate (mesh-0) and mesh-1 are depicted in Fig. 10a. As observed in Fig. 10a, mesh-0 does not show obvious redox peaks related to hydrogen adsorption/desorption. In contrast, the CV profile of mesh-1 presented in the cathodic and anodic direction, which shows reduction (C_1) and oxidation (A_1) peaks, attributed to hydrogen adsorption and desorption, respectively, indicates that GO serves as a hydrogen storage material [95].

In Fig. 10b, mesh-2 acts as a catalyst for the decomposition of water and storage of the hydrogen released from water. In the cathodic direction, according to the obvious peak (C_1) around −1.2 V, water decomposition, hydrogen formation and adsorption have taken place [40]. In the anodic direction, there is a clear peak at −0.6 V (A_1) related to hydrogen desorption from the surface [40,96]. This CV profile is in good agreement with the reported hydrogen storage capacity using rGO-ZrO_2 [40], but a significant increase of about two-fold is observed. Gradually, the heights of C_1 and A_1 increase and as time passes, more hydrogen atoms are adsorbed and desorbed from the surface of electrodes, respectively.

The CV profile of mesh-3 in Fig. 10c shows that hydrogen adsorption/desorption has been carried out in an alkaline medium on the surface of the electrode. The cathodic excursion span exhibits one major peak (C_1) associated with hydrogen production and adsorption. Meanwhile, the reverse potential scan is characterized by a noticeable anodic current peak (A_1) attributed to hydrogen desorption. After 20 cycles, the potential of C_1 was shifted to a negative potential. Conversely, A_1 was moved to a positive potential while the height of C_1 and A_1 steadily increased. These cathodic and anodic peaks reveal that the resultant electrodes are qualified candidates for hydrogen production and

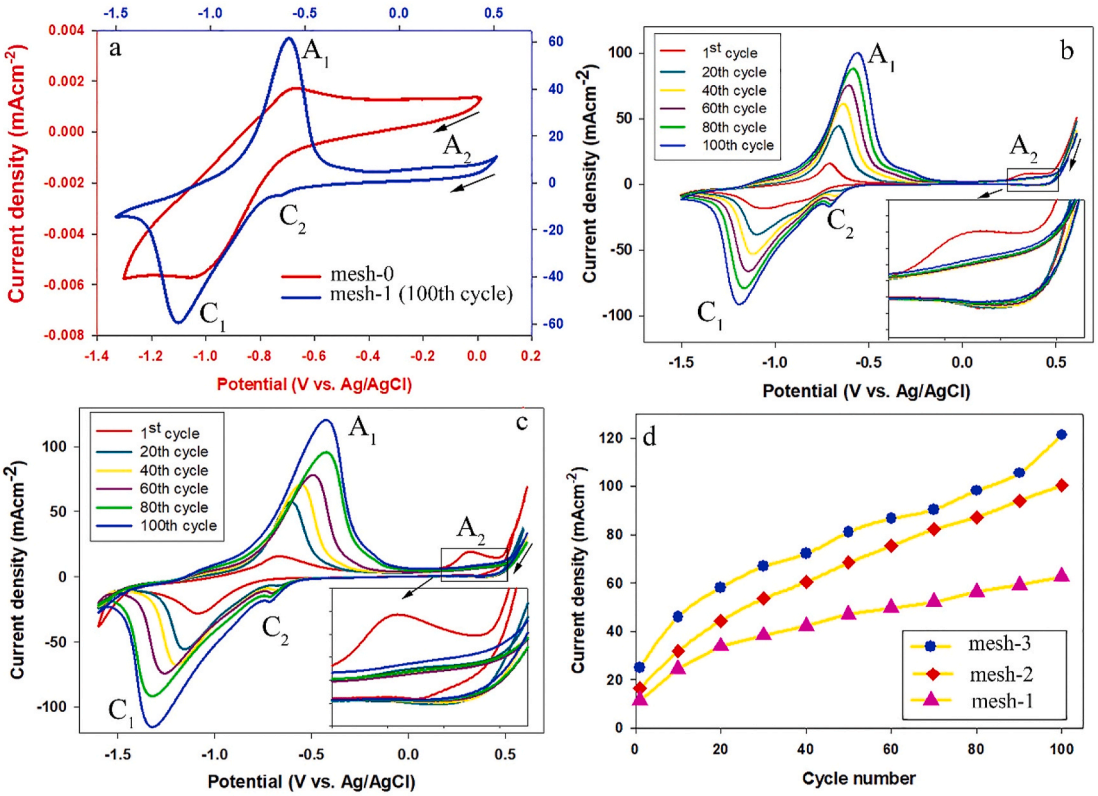

Fig. 10. The CV profile of (a) mesh-0 and mesh-1, (b) mesh-2, (c) mesh-3 and (d) comparison of the current density of A_1 (j_{A1}) as a function of cycle's number. The inset photo of b and c, depicts a clear photo of A_2 peaks.

adsorption on the surface of nanocomposites, which offer host sites for hydrogen adsorption and desorption.

Meticulously examining the CV profiles exhibits two minor peaks in the anodic (A_2) and cathodic (C_2) directions. The second anodic peak (A_2) is located on 0.2 V for all the samples and is likely referred to the oxidation of hydrogen atoms [95,97–99]. After the second cycle, another negligible peak (C_2) around −0.6 V appears, probably down to the reduction of hydrogen atoms or oxide groups of GO [95,98,100], which is a redox pair of A_2.

To visualize ZrO_2 and Au effect on hydrogen adsorption/desorption mechanism, the current density of the oxidation peak (j_{A1}) of the samples was plotted as a function of cycle number (Fig. 10d). The amount of j_{A1} of GO has risen about two folds by adding ZrO_2 NPs, which is beneficial for hydrogen storage because metal oxide increases the surface area and host site. As observed in Fig. 10d, the addition of Au NPs on the surface of GO-ZrO_2 significantly increases j_{A1} value, confirming the critical role of Au NPs in this issue. The enhanced j_{A1} can likely be justified as follows: the presence of the metal and metal oxide NPs is an obvious advantage because hydrogen spillover mechanism on carbonaceous material improves hydrogen adsorption [10,40,101,102]. Here, Au and ZrO_2 NPs help hydrogen to diffuse on the mesh-3 surface through carbon bridges and store between GO sheets. High surface area and porous structure provided by ZrO_2 and Au NPs immobilization endow more opportunity to adsorb hydrogen on the surface [88]. Additionally, the presence of oxygen-containing functional groups contributes to the facilitation of adsorption and stabilization of adsorbed hydrogen atoms by increasing the interaction between metal NPs and substrates [10,15,103].

The integration of the anodic peak, where hydrogen atoms are being desorbed, is a gauge of total charge correlated with hydrogen desorption from the surface. To scrutinize the total hydrogen charge, equation (5) was used for each cycle by designating a baseline to separate the double layer and the faradaic region. The potential range, I_a and I_{dl} were chosen by the CV profile. The anodic area of the first cycle is depicted in Fig. 11a. The dotted and white areas show the double layer capacitance and the amount of hydrogen desorption, respectively. Using equation (5) and CV data, the amount of hydrogen desorption was estimated and is shown as a function of the cycle number in Fig. 11b. The results suggest that the Q_H has been gradually promoted by increasing the cycle number up to the 154th cycle, probably down to the creation of a new host site by cycling [104,105]. The amount of Q_H from the 154th to 167th was almost steady and a sharp decline happened after the 167th cycle. The decreasing may be due to the surface oxidation of the electrode, which leads to the degraded host site of the electrode, thereby decreasing hydrogen adsorption.

The morphological characteristic of mesh-3 was illustrated by SEM analysis before and after hydrogen storage investigation and is depicted in Fig. 12. The images show no substantial changes in the morphology after the electrochemical test. However, a meticulous survey suggests that the rough structure turns to a slightly smooth surface after 200 electrochemical cycles in Fig. 12c and d. As the data show, roughness has an obvious effect on the electrochemical study [106]. Thus, decreasing hydrogen storage is partially the courtesy of the change in the morphology.

2.9. Proposed mechanism for the electrochemical hydrogen storage

Based on the present observations and other reports [40,101,107], the proposed mechanism for hydrogen adsorption and desorption at the mesh-3 is schematized in Fig. 13. The proposed mechanism is based on the electrochemical reactions on the surface of mesh-3, as follows:

Applying potential leads to water decomposition (Volmer reaction, Eq. (6)). Consequently, H atoms tend to migrate and adsorb on the working electrode surface (Fig. 13a).

$$\text{mesh-3} + xH_2O + xe^- \rightarrow \text{mesh-3-}xH + xOH^- \quad (6)$$

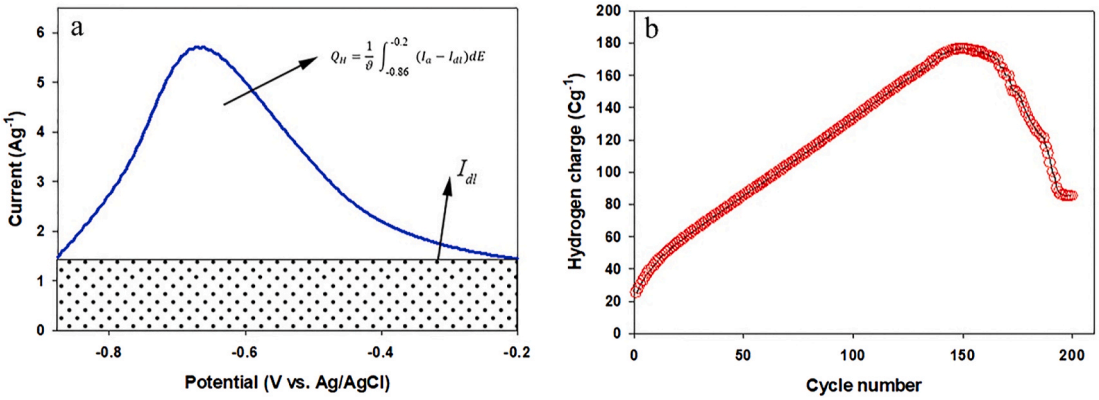

Fig. 11. (a) A presentation of A_1 area of mesh-3 (the first cycle) in 1 M KOH and (b) cyclic life performance of mesh-3 as a function of the cycle's number.

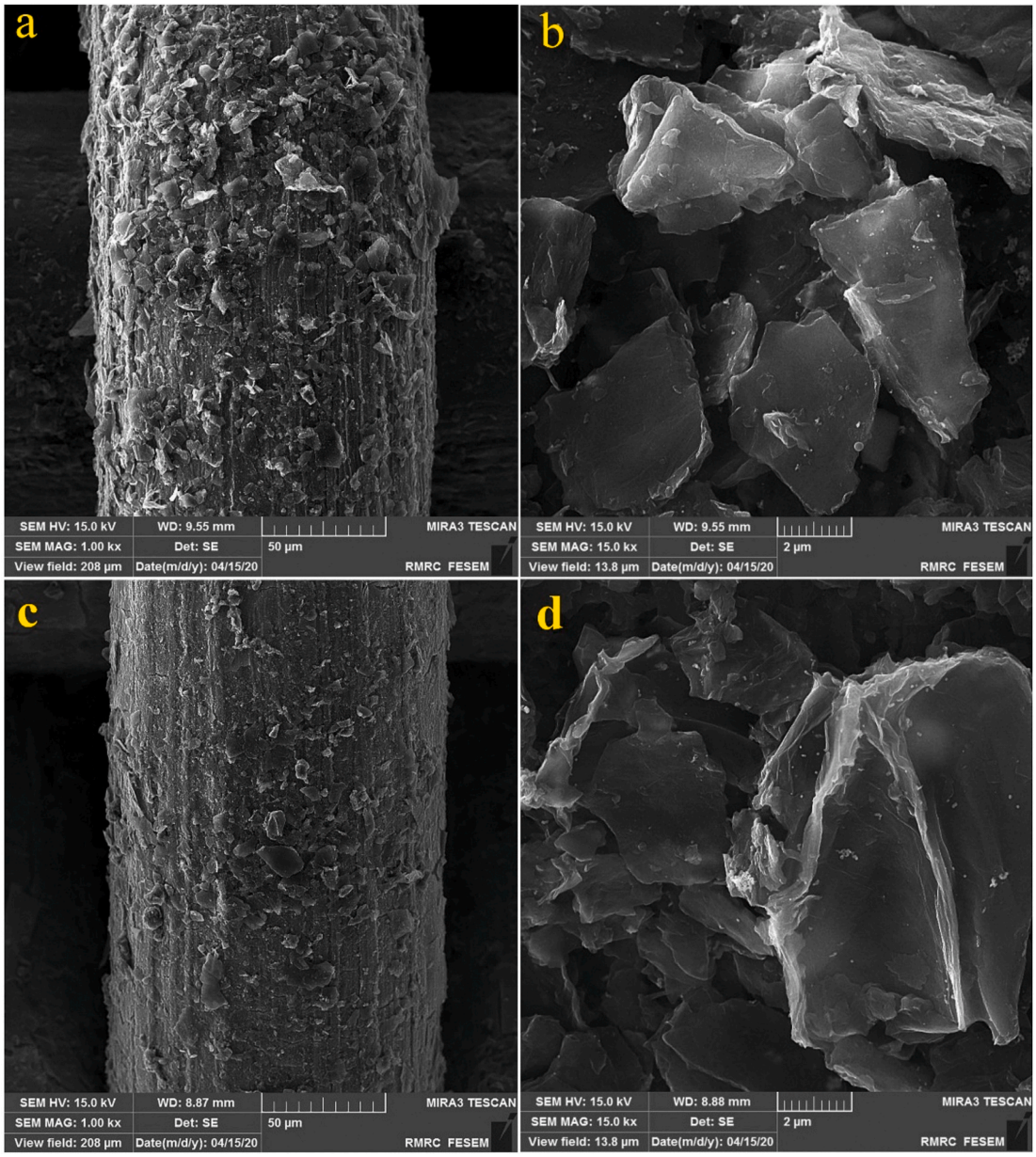

Fig. 12. The SEM images of mesh-3 with different magnification (a and b) before and (c and d) after 200 cyclic voltammetry in 1 M KOH at 0.1 V/S sweep rate.

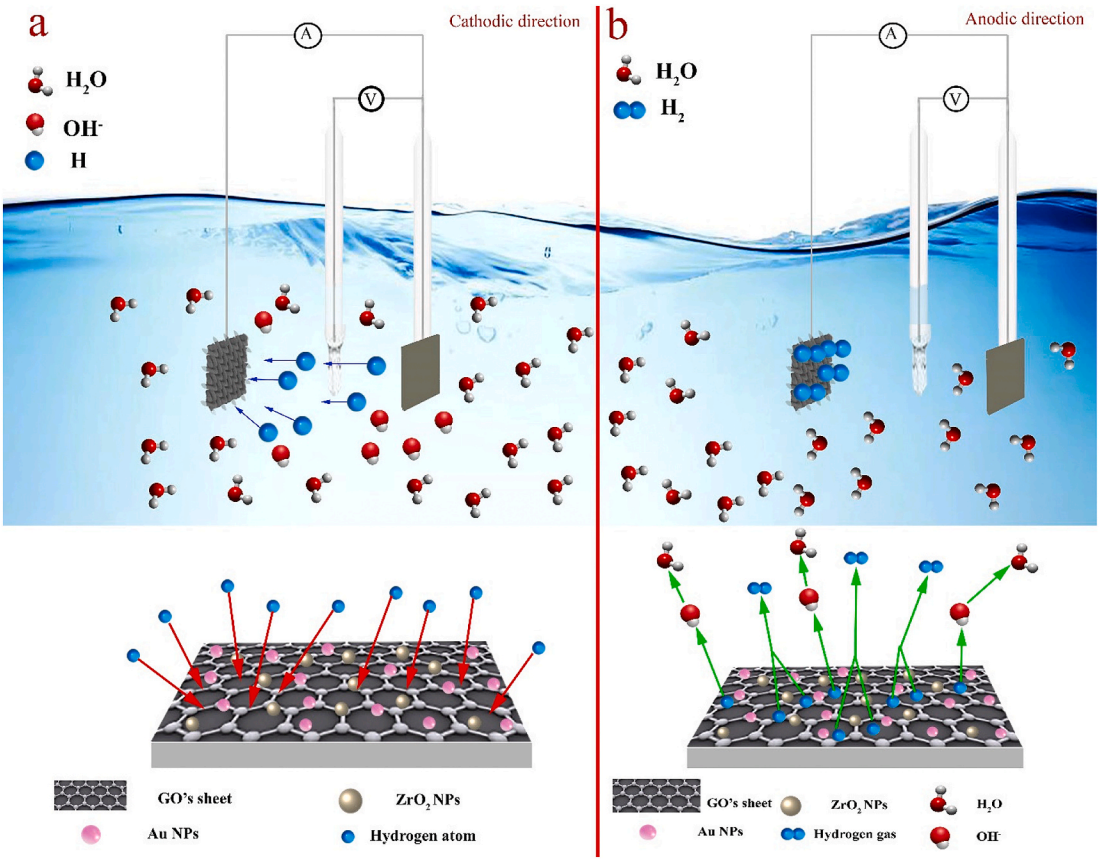

Fig. 13. A schematic illustration of the electrochemical cell during (a) cathodic and (b) anodic direction. The size of atoms is overestimated for convenience.

The adsorbed hydrogen atoms can react with each other or OH^- to produce hydrogen gas (Eq. (7)) or water (Eq. (8)) [107], respectively (Fig. 13b).

$$2\text{mesh-3-xH} \rightarrow 2\text{mesh-3} + x\text{H}_2 \quad (7)$$

$$\text{mesh-3-xH} + x\text{OH}^- \rightarrow \text{mesh-3} + x\text{H}_2\text{O} + x\text{e}^- \quad (8)$$

The production hydrogen gas (Eq. (7)) was physically observed by bubbles.

3. Conclusion

Graphene oxide (GO) was modified by commercial zirconium oxide (ZrO_2) to investigate the influence of metal oxide on hydrogen adsorption and storage performance. Furthermore, LAL was used to synthesize Au NPs in deionized water and load on pre-synthesized nanocomposite (GO-ZrO_2) to attain high hydrogen storage capacity. Finally, the surface of the nanocomposite was elucidated viz. XRD, FTIR, XPS, BET, SEM, TEM, HRTEM, EDX and elemental mapping. According to BET analysis, after loading Au NPs, a significant increase of surface area could contribute to better interaction between the electrode and medium. Hydrogen adsorption was scrutinized to determine the effects of ZrO_2 and Au NPs. The comparison of the CV profiles indicated that ZrO_2 and Au NPs positively affect the current density, increasing it to about 66% and 30%, respectively. The stability of the best resultant electrode, mesh-3, was examined during 200 cycles and the SEM analysis of the surface of the electrode shows it is slightly smoother.

Author statement

All persons who have made substantial contributions to the work reported in the manuscript (e.g., technical help, writing and editing assistance, general support), but who do not meet the criteria for authorship, are named in the Acknowledgements and have given us their written permission to be named. If we have not included an Acknowledgements, then that indicates that we have not received substantial contributions from non-authors.

Declaration of competing interest

The authors declare that they have no known competing financial interests or personal relationships that could have appeared to influence the work reported in this paper.

Acknowledgments

We gratefully acknowledge the Bu-Ali Sina University for the support of this work.

References

[1] B. Feizi Mohazzab, B. Jaleh, M. Nasrollahzadeh, S. Khazalpour, M. Sajjadi, R. S. Varma, Upgraded valorization of biowaste: laser-assisted synthesis of Pd/calcium lignosulfonate nanocomposite for hydrogen storage and environmental remediation, ACS Omega 5 (11) (2020) 5888–5899.
[2] H. Wang, H. Zhang, Z. Wang, X. Xia, Y. Bao, K. Homewood, M.d.A. Lourenço, G. Shao, Y. Gao, In-situ hydrogen production and storage in (002) oriented TiO_2 thin films, Appl. Surf. Sci. 509 (2020), 145366.
[3] L. Grinberga, J. Hodakovska, J. Kleperis, G. Vaivars, J. Klavins, Electrochemical hydrogen storage and usage aspects: nickel electrode in acidic electrolyte, Russ. J. Electrochem. 43 (2007) 598–602.
[4] N. Rusman, M. Dahari, A review on the current progress of metal hydrides material for solid-state hydrogen storage applications, Int. J. Hydrogen Energy 41 (2016) 12108–12126.
[5] K. Shashikala, Hydrogen storage materials, functional materials preparation, Process. Appl 15 (2012) 607–637.
[6] A.J. Lachawiec, G. Qi, R.T. Yang, Hydrogen storage in nanostructured carbons by spillover: bridge-building enhancement, Langmuir 21 (2005) 11418–11424.

[7] Y. Li, R.T. Yang, Hydrogen storage in low silica type X zeolites, J. Phys. Chem. B 110 (2006) 17175–17181.
[8] Y. Li, R.T. Yang, Significantly enhanced hydrogen storage in metal−organic frameworks via spillover, J. Am. Chem. Soc. 128 (2006) 726–727.
[9] Y. Li, R.T. Yang, Hydrogen storage in metal−organic frameworks by bridged hydrogen spillover, J. Am. Chem. Soc. 128 (2006) 8136–8137.
[10] L. Wang, R.T. Yang, Hydrogen storage on carbon-based adsorbents and storage at ambient temperature by hydrogen spillover, Catal. Rev. 52 (2010) 411–461.
[11] L. Wang, R.T. Yang, Hydrogen storage properties of carbons doped with ruthenium, platinum, and nickel nanoparticles, J. Phys. Chem. C 112 (2008) 12486–12494.
[12] K.-Y. Lin, W.-T. Tsai, T.-J. Yang, Effect of Ni nanoparticle distribution on hydrogen uptake in carbon nanotubes, J. Power Sources 196 (2011) 3389–3394.
[13] C.-K. Back, G. Sandí, J. Prakash, J. Hranisavljevic, Hydrogen sorption on palladium-doped sepiolite-derived carbon nanofibers, J. Phys. Chem. B 110 (2006) 16225–16231.
[14] B.-J. Kim, Y.-S. Lee, S.-J. Park, Preparation of platinum-decorated porous graphite nanofibers, and their hydrogen storage behaviors, J. Colloid Interface Sci. 318 (2008) 530–533.
[15] L. Wang, F.H. Yang, R.T. Yang, M.A. Miller, Effect of surface oxygen groups in carbons on hydrogen storage by spillover, Ind. Eng. Chem. Res. 48 (2009) 2920–2926.
[16] J. Carter, P. Lucchesi, P. Corneil, D. Yates, J. Sinfelt, Exchange of deuterium with the hydroxyl groups of alumina, J. Phys. Chem. 69 (1965) 3070–3074.
[17] Q. Li, A.D. Lueking, Effect of surface oxygen groups and water on hydrogen spillover in Pt-doped activated carbon, J. Phys. Chem. C 115 (2011) 4273–4282.
[18] W.J. Ambs, A. Wj, M. Mm JR., Hydrogen Spillover on Platinum-Alumina, Effect of Water, 1983.
[19] J. Miller, B. Meyers, F. Modica, G. Lane, M. Vaarkamp, D. Koningsberger, Hydrogen temperature-programmed desorption (H_2 TPD) of supported platinum catalysts, J. Catal. 143 (1993) 395–408.
[20] A.C. Cooper, G.P. Pez, Hydrogen storage using carbon-metal hybrid compositions, in: Google Patents, 2003.
[21] A. Lueking, R.T. Yang, Hydrogen spillover from a metal oxide catalyst onto carbon nanotubes—implications for hydrogen storage, J. Catal. 206 (2002) 165–168.
[22] P.T. Ahmad, B. Jaleh, M. Nasrollahzadeh, Z. Issaabadi, Efficient reduction of waste water pollution using GO/γMnO_2/Pd nanocomposite as a highly stable and recoverable catalyst, Separ. Purif. Technol. 225 (2019) 33–40.
[23] B. Feizi Mohazzab, B. Jaleh, M. Nasrollahzadeh, Z. Issaabadi, R.S. Varma, Laser ablation-assisted synthesis of GO/TiO_2/Au nanocomposite: applications in K_3[Fe$(CN)_6$] and Nigrosin reduction, Mol. Catal. 473 (2019), 110401.
[24] T. Kuila, A.K. Mishra, P. Khanra, N.H. Kim, J.H. Lee, Recent advances in the efficient reduction of graphene oxide and its application as energy storage electrode materials, Nanoscale 5 (2013) 52–71.
[25] K. Sekar, G. Raji, L. Tong, Y. Zhu, S. Liu, R. Xing, Boosting the electrochemical performance of MoS_2 nanospheres-N-doped-GQDs-rGO three-dimensional nanostructure for energy storage and conversion applications, Appl. Surf. Sci. 504 (2020), 144441.
[26] M.D. Ganji, S. Emami, A. Khosravi, M. Abbasi, Si-decorated graphene: a promising media for molecular hydrogen storage, Appl. Surf. Sci. 332 (2015) 105–111.
[27] P. Bénard, R. Chahine, Modeling of adsorption storage of hydrogen on activated carbons, Int. J. Hydrogen Energy 26 (2001) 849–855.
[28] S.H. Aboutalebi, S. Aminorroaya-Yamini, I. Nevirkovets, K. Konstantinov, H. K. Liu, Enhanced hydrogen storage in graphene oxide-MWCNTs composite at room temperature, Adv. Energy Mater. 2 (2012) 1439–1446.
[29] C.-C. Huang, N.-W. Pu, C.-A. Wang, J.-C. Huang, Y. Sung, M.-D. Ger, Hydrogen storage in graphene decorated with Pd and Pt nano-particles using an electroless deposition technique, Separ. Purif. Technol. 82 (2011) 210–215.
[30] V.B. Parambhath, R. Nagar, S. Ramaprabhu, Effect of nitrogen doping on hydrogen storage capacity of palladium decorated graphene, Langmuir 28 (2012) 7826–7833.
[31] Y. Wang, C.X. Guo, X. Wang, C. Guan, H. Yang, K. Wang, C.M. Li, Hydrogen storage in a Ni–B nanoalloy-doped three-dimensional graphene material, Energy Environ. Sci. 4 (2011) 195–200.
[32] E.S. Cho, A.M. Ruminski, S. Aloni, Y.-S. Liu, J. Guo, J.J. Urban, Graphene oxide/metal nanocrystal multilaminates as the atomic limit for safe and selective hydrogen storage, Nat. Commun. 7 (2016) 1–8.
[33] G. Wu, J. Li, C. Tang, T. Ouyang, C. He, C. Zhang, J. Zhong, A comparative investigation of metal (Li, Ca and Sc)-decorated 6, 6, 12-graphyne monolayers and 6, 6, 12-graphyne nanotubes for hydrogen storage, Appl. Surf. Sci. 498 (2019), 143763.
[34] N. Naseri, S. Ghasemi, M. Pourreza, A. Moshfegh, Sustainable starfish like cobalt electrocatalyst grown on optimized CNT-graphene hybrid host for efficient water oxidation, Appl. Surf. Sci. (2020), 146391.
[35] Z. Li, D. Wu, Y. Ouyang, H. Wu, M. Jiang, F. Wang, L.Y. Zhang, Synthesis of hollow cobalt phosphide nanocrystals with ultrathin shells anchored on reduced graphene oxide as an electrocatalyst toward hydrogen evolution, Appl. Surf. Sci. 506 (2020), 144975.
[36] J. Zhao, D. Zhang, F. Guo, H. Guo, Y. Liu, Y. Yin, H. Hu, X. Wang, Facile one-pot supercritical synthesis of MoS_2/pristine graphene nanohybrid as a highly active advanced electrocatalyst for hydrogen evolution reaction, Appl. Surf. Sci. (2020), 147282.
[37] R. Krishna, E. Titus, L.C. Costa, J.C. Menezes, M.R. Correia, S. Pinto, J. Ventura, J. Araújo, J.A. Cavaleiro, J.J. Gracio, Facile synthesis of hydrogenated reduced graphene oxide via hydrogen spillover mechanism, J. Mater. Chem. 22 (2012) 10457–10459.
[38] V. Jain, B. Kandasubramanian, Functionalized graphene materials for hydrogen storage, J. Mater. Sci. (2020) 1–39.
[39] W. Zhang, Z. Zhang, F. Zhang, W. Yang, Ti-decorated graphitic-C_3N_4 monolayer: a promising material for hydrogen storage, Appl. Surf. Sci. 386 (2016) 247–254.
[40] M. Kaur, K. Pal, An investigation for hydrogen storage capability of zirconia-reduced graphene oxide nanocomposite, Int. J. Hydrogen Energy 41 (2016) 21861–21869.
[41] M. Onyszko, K. Urbas, M. Aleksandrzak, E. Mijowska, Reduced graphene oxide and inorganic nanoparticles composites–synthesis and characterization, Pol. J. Chem. Technol. 17 (2015) 95–103.
[42] S.-R. Yan, T. Gholami, O. Amiri, M. Salavati-Niasari, S. Seifi, M. Amiri, M. Sabet, L.K. Foong, Effect of adding TiO_2, SiO_2 and graphene on of electrochemical hydrogen storage performance and coulombic efficiency of $CoAl_2O_4$ spinel, J. Alloys Compd. 828 (2020), 154353.
[43] P. Pei, M.B. Whitwick, S. Kureshi, M. Cannon, G. Quan, E. Kjeang, Hydrogen storage mechanism in transition metal decorated graphene oxide: the symbiotic effect of oxygen groups and high layer spacing, Int. J. Hydrogen Energy 45 (2020) 6713–6726.
[44] Y. Zhang, Y. Ji, W. Zhang, F. Hu, Y. Qi, D. Zhao, Electrochemical hydrogen storage behaviors of as-milled Mg-Ce-Ni-Al-based alloys applied to Ni-MH battery, Appl. Surf. Sci. 494 (2019) 170–178.
[45] W.L.N. Bandara, R.M. de Silva, K.N. de Silva, D. Dahanayake, S. Gunasekara, K. Thanabalasingam, Is nano ZrO_2 a better photocatalyst than nano TiO_2 for degradation of plastics? RSC Adv. 7 (2017) 46155–46163.
[46] S. Jo, P. Verma, Y. Kuwahara, K. Mori, W. Choi, H. Yamashita, Enhanced hydrogen production from ammonia borane using controlled plasmonic performance of Au nanoparticles deposited on TiO_2, J. Mater. Chem. 5 (2017) 21883–21892.
[47] H.-S. Kim, H. Lee, K.-S. Han, J.-H. Kim, M.-S. Song, M.-S. Park, J.-Y. Lee, J.-K. Kang, Hydrogen storage in Ni nanoparticle-dispersed multiwalled carbon nanotubes, J. Phys. Chem. B 109 (2005) 8983–8986.
[48] E. Yoo, L. Gao, T. Komatsu, N. Yagai, K. Arai, T. Yamazaki, K. Matsuishi, T. Matsumoto, J. Nakamura, Atomic hydrogen storage in carbon nanotubes promoted by metal catalysts, J. Phys. Chem. B 108 (2004) 18903–18907.
[49] L. Ma, J.-M. Zhang, K.-W. Xu, Hydrogen storage on nitrogen induced defects in palladium-decorated graphene: a first-principles study, Appl. Surf. Sci. 292 (2014) 921–927.
[50] Y. Wang, Z. Meng, Y. Liu, D. You, K. Wu, J. Lv, X. Wang, K. Deng, D. Rao, R. Lu, Lithium decoration of three dimensional boron-doped graphene frameworks for high-capacity hydrogen storage, Appl. Phys. Lett. 106 (2015), 063901.
[51] Y.-J. Han, S.-J. Park, Influence of nickel nanoparticles on hydrogen storage behaviors of MWCNTs, Appl. Surf. Sci. 415 (2017) 85–89.
[52] V. Mani, B.V. Chikkaveeraiah, V. Patel, J.S. Gutkind, J.F. Rusling, Ultrasensitive immunosensor for cancer biomarker proteins using gold nanoparticle film electrodes and multienzyme-particle amplification, ACS Nano 3 (2009) 585–594.
[53] L. Cheng, D. Zhang, Y. Liao, F. Li, H. Zhang, Q. Xiang, Constructing functionalized plasmonic gold/titanium dioxide nanosheets with small gold nanoparticles for efficient photocatalytic hydrogen evolution, J. Colloid Interface Sci. 555 (2019) 94–103.
[54] Y.-J. Kim, J. Park, H.S. Jeong, M. Park, S. Baik, D.S. Lee, H. Rho, H. Kim, J.H. Lee, S.-M. Kim, A seed-mediated growth of gold nanoparticles inside carbon nanotube fibers for fabrication of multifunctional nanohybrid fibers with enhanced mechanical and electrical properties, Nanoscale 11 (2019) 5295–5303.
[55] W. Zhu, X. Li, W. Liu, Z. Chen, J. Li, H. Pan, In situ growth of gold nanoparticles based on simultaneous green reduction by methylene blue for non-enzymatic glucose sensing, Int. J. Electrochem. Sci 12 (2017) 4970–4978.
[56] B. Jaleh, S. Karami, M. Sajjadi, B.F. Mohazzab, S. Azizian, M. Nasrollahzadeh, R. S. Varma, Laser-assisted preparation of Pd nanoparticles on carbon cloth for the degradation of environmental pollutants in aqueous medium, Chemosphere 246 (2020), 125755.
[57] A. Serkov, E. Barmina, A. Simakin, P. Kuzmin, V. Voronov, G. Shafeev, Generation of core–shell nanoparticles Al@Ti by laser ablation in liquid for hydrogen storage, Appl. Surf. Sci. 348 (2015) 71–74.
[58] C.L. Sajti, R. Sattari, B.N. Chichkov, S. Barcikowski, Gram scale synthesis of pure ceramic nanoparticles by laser ablation in liquid, J. Phys. Chem. C 114 (2010) 2421–2427.
[59] S. Barcikowski, G. Compagnini, Advanced nanoparticle generation and excitation by lasers in liquids, Phys. Chem. Chem. Phys. 15 (2013) 3022–3026.
[60] R. Streubel, S. Barcikowski, B. Gökce, Continuous multigram nanoparticle synthesis by high-power, high-repetition-rate ultrafast laser ablation in liquids, Opt. Lett. 41 (2016) 1486–1489.
[61] P. Wagener, J. Jakobi, S. Barcikowski, Organic nanoparticles generated by combination of laser fragmentation and ultrasonication in liquid, J. Laser Micro/Nanoeng. 6 (2011).
[62] S. Kohsakowski, A. Santagata, M. Dell'Aglio, A. de Giacomo, S. Barcikowski, P. Wagener, B. Gökce, High productive and continuous nanoparticle fabrication by laser ablation of a wire-target in a liquid jet, Appl. Surf. Sci. 403 (2017) 487–499.
[63] I. Corni, M.P. Ryan, A.R. Boccaccini, Electrophoretic deposition: from traditional ceramics to nanotechnology, J. Eur. Ceram. Soc. 28 (2008) 1353–1367.
[64] B. Jaleh, K. Shariati, M. Khosravi, A. Moradi, S. Ghasemi, S. Azizian, Uniform and stable electrophoretic deposition of graphene oxide on steel mesh: low temperature thermal treatment for switching from superhydrophilicity to

superhydrophobicity, Colloid. Surface. Physicochem. Eng. Aspect. 577 (2019) 323–332.
[65] A.A. Daryakenari, D. Hosseini, T. Saito, A. Apostoluk, C.R. Müller, J.-J. Delaunay, Ethanol electro-oxidation on nanoworm-shaped Pd particles supported by nanographitic layers fabricated by electrophoretic deposition, RSC Adv. 5 (2015), 52578-52587.
[66] W.S. Hummers Jr., R.E. Offeman, Preparation of graphitic oxide, J. Am. Chem. Soc. 80 (1958), 1339-1339.
[67] Q. Zhou, J. Huang, J. Wang, Z. Yang, S. Liu, Z. Wang, S. Yang, Preparation of a reduced graphene oxide/zirconia nanocomposite and its application as a novel lubricant oil additive, RSC Adv. 5 (2015) 91802–91812.
[68] H.E. Swanson, Standard X-Ray Diffraction Powder Patterns: Data for 70 Substances, US Department of Commerce, National Bureau of Standards, 1974.
[69] P. Scherrer, Determination of the internal structure and size of colloid particles by X-rays, Colloid Chem. Textbook (1912) 387–409.
[70] A.M. Keene, K.M. Tyner, Analytical characterization of gold nanoparticle primary particles, aggregates, agglomerates, and agglomerated aggregates, J. Nanoparticle Res. 13 (2011) 3465–3481.
[71] A.F.V. da Silva, A.P. Fagundes, D.L.P. Macuvele, E.F.U. de Carvalho, M. Durazzo, N. Padoin, C. Soares, H.G. Riella, Green synthesis of zirconia nanoparticles based on Euclea natalensis plant extract: optimization of reaction conditions and evaluation of adsorptive properties, Colloid. Surface. Physicochem. Eng. Aspect. 583 (2019), 123915.
[72] N. Horti, M. Kamatagi, S. Nataraj, M. Wari, S. Inamdar, Structural and optical properties of zirconium oxide (ZrO_2) nanoparticles: effect of calcination temperature, Nano Express 1 (2020), 010022.
[73] G.-Y. Guo, Y.-L. Chen, W.-J. Ying, Thermal, spectroscopic and X-ray diffractional analyses of zirconium hydroxides precipitated at low pH values, Mater. Chem. Phys. 84 (2004) 308–314.
[74] L.A. Pérez-Maqueda, E. Matijević, Preparation and characterization of nanosized zirconium (hydrous) oxide particles, J. Mater. Res. 12 (1997) 3286–3292.
[75] S. Naghdi, B. Jaleh, A. Ehsani, Electrophoretic deposition of graphene oxide on aluminum: characterization, low thermal annealing, surface and anticorrosive properties, Bull. Chem. Soc. Jpn. 88 (2015) 722–728.
[76] K. Gurushantha, K. Anantharaju, L. Renuka, S. Sharma, H. Nagaswarupa, S. Prashantha, Y. Vidya, H. Nagabhushana, New green synthesized reduced graphene oxide–ZrO_2 composite as high performance photocatalyst under sunlight, RSC Adv. 7 (2017) 12690–12703.
[77] N. Díez, A. Śliwak, S. Gryglewicz, B. Grzyb, G. Gryglewicz, Enhanced reduction of graphene oxide by high-pressure hydrothermal treatment, RSC Adv. 5 (2015) 81831–81837.
[78] V. Amendola, G.A. Rizzi, S. Polizzi, M. Meneghetti, Synthesis of gold nanoparticles by laser ablation in toluene: quenching and recovery of the surface plasmon absorption, J. Phys. Chem. B 109 (2005) 23125–23128.
[79] R.M. Baiee, Generation of Ultra-fine Nanoparticles by Laser Ablation in Liquid, The University of Manchester, United Kingdom), 2019.
[80] K.S. Sing, R.T. Williams, Physisorption hysteresis loops and the characterization of nanoporous materials, Adsorpt. Sci. Technol. 22 (2004) 773–782.
[81] J. Rouquerol, F. Rouquerol, P. Llewellyn, G. Maurin, K.S. Sing, Adsorption by Powders and Porous Solids: Principles, Methodology and Applications, Academic press, 2013.
[82] S. Kalidhasan, A.S.K. Kumar, V. Rajesh, N. Rajesh, The journey traversed in the remediation of hexavalent chromium and the road ahead toward greener alternatives—a perspective, Coord. Chem. Rev. 317 (2016) 157–166.
[83] A. Reyhani, S.Z. Mortazavi, S. Mirershadi, A.N. Golikand, A.Z. Moshfegh, H2 adsorption mechanism in Mg modified multi-walled carbon nanotubes for hydrogen storage, Int. J. Hydrogen Energy 37 (2012) 1919–1926.
[84] A.E.-A.A. Said, M.M.A. El-Wahab, M.A. El-Aal, Catalytic dehydration of methanol to dimethyl ether over nanosized WO_3/Al_2O_3 system under inert and oxidative atmosphere, Monatshefte für Chemie-Chemical Monthly 147 (2016) 1507–1516.
[85] A.E.-A.A. Said, M.M. Abd El-Wahab, M. Abd El-Aal, Catalytic dehydration of methanol to dimethyl ether over nanosized WO_3/Al_2O_3 system under inert and oxidative atmosphere, Monatshefte für Chemie-Chemical Monthly 147 (2016) 1507–1516.
[86] K. Al-Attafi, A. Nattestad, Y. Yamauchi, S.X. Dou, J.H. Kim, Aggregated mesoporous nanoparticles for high surface area light scattering layer TiO_2 photoanodes in Dye-sensitized Solar Cells, Sci. Rep. 7 (2017) 1–8.
[87] V. Jiménez, A. Ramírez-Lucas, P. Sánchez, J.L. Valverde, A. Romero, Hydrogen storage in different carbon materials: influence of the porosity development by chemical activation, Appl. Surf. Sci. 258 (2012) 2498–2509.
[88] A. Salehabadi, M.I. Ahmad, N. Morad, M. Salavati-Niasari, M. Enhessari, Electrochemical hydrogen storage properties of $Ce_{0.75}Zr_{0.25}O_2$ nanopowders synthesized by sol-gel method, J. Alloys Compd. 790 (2019) 884–890.
[89] F. Liu, S. Song, D. Xue, H. Zhang, Folded structured graphene paper for high performance electrode materials, Adv. Mater. 24 (2012) 1089–1094.
[90] A.M. Mostafa, E.A. Mwafy, Synthesis of ZnO and Au@ZnO core/shell nano-catalysts by pulsed laser ablation in different liquid media, J. Mater. Res. Technol. 9 (3) (2020) 3241–3248.
[91] H. McMurdie, M. Morris, E. Evans, B. Paretzkin, W. Wong-Ng, L. Ettlinger, C. Hubbart, ZnO reference for bragg peak position and net constants, Powder Diffr. 1 (1986) 76.
[92] J.t. McCullough, K. Trueblood, The crystal structure of baddeleyite (monoclinic ZrO_2), Acta Crystallogr. 12 (1959) 507–511.
[93] K. Jurewicz, E. Frackowiak, F. Béguin, Towards the mechanism of electrochemical hydrogen storage in nanostructured carbon materials, Appl. Phys. A 78 (2004) 981–987.
[94] F. Nart, W. Vielstich, Noramlization of Porous Active Surfaces, Handbook of Fuel Cells, 2010.
[95] G. Guo, H. Huang, F. Xue, C. Liu, H. Yu, X. Quan, X. Dong, Electrochemical hydrogen storage of the graphene sheets prepared by DC arc-discharge method, Surf. Coating. Technol. 228 (2013) S120–S125.
[96] C. Wen, Y. Wei, D. Tang, B. Sa, T. Zhang, C. Chen, Improving the electrocatalytic properties of Pd-based catalyst for direct alcohol fuel cells: effect of solid solution, Sci. Rep. 7 (2017) 1–11.
[97] X. Chen, X. Gao, H. Zhang, Z. Zhou, W. Hu, G. Pan, H. Zhu, T. Yan, D. Song, Preparation and electrochemical hydrogen storage of boron nitride nanotubes, J. Phys. Chem. B 109 (2005) 11525–11529.
[98] E. Liu, J. Wang, J. Li, C. Shi, C. He, X. Du, N. Zhao, Enhanced electrochemical hydrogen storage capacity of multi-walled carbon nanotubes by TiO_2 decoration, Int. J. Hydrogen Energy 36 (2011) 6739–6743.
[99] Y. Yu, N. Zhao, C. Shi, C. He, E. Liu, J. Li, Electrochemical hydrogen storage of expanded graphite decorated with TiO_2 nanoparticles, Int. J. Hydrogen Energy 37 (2012) 5762–5768.
[100] J.B. Martin, I.A. Kinloch, R.A. Dryfe, Are carbon nanotubes viable materials for the electrochemical storage of hydrogen? J. Phys. Chem. C 114 (2010) 4693–4703.
[101] M.S. Morassaei, A. Salehabadi, M. Salavati-Niasari, A. Akbari, Preparation, structural analysis, and assessing the impacts of holmium and ytterbium on electrochemical hydrogen storage property of strontium cerium molybdate nanostructures, Electrochim. Acta 356 (2020), 136851.
[102] M. Kaur, K. Pal, Potential Electrochemical Hydrogen Storage in Nickel and Cobalt Nanoparticles-Induced Zirconia-Graphene Nanocomposite.
[103] A.D. Lueking, R.T. Yang, Hydrogen spillover to enhance hydrogen storage—study of the effect of carbon physicochemical properties, Appl. Catal. Gen. 265 (2004) 259–268.
[104] F.S. Sangsefidi, M. Salavati-Niasari, Thermal decomposition synthesis, characterization and electrochemical hydrogen storage characteristics of Co_3O_4–CeO_2 porous nanocomposite, Int. J. Hydrogen Energy 42 (2017) 20071–20081.
[105] T. Gholami, M. Salavati-Niasari, Effects of copper: aluminum ratio in CuO/Al_2O_3 nanocomposite: electrochemical hydrogen storage capacity, band gap and morphology, Int. J. Hydrogen Energy 41 (2016) 15141–15148.
[106] D. Menshykau, I. Streeter, R.G. Compton, Influence of electrode roughness on cyclic voltammetry, J. Phys. Chem. C 112 (2008) 14428–14438.
[107] B. Sarac, V. Zadorozhnyy, E. Berdonosova, Y.P. Ivanov, S. Klyamkin, S. Gumrukcu, A.S. Sarac, A. Korol, D. Semenov, M. Zadorozhnyy, Hydrogen storage performance of the multi-principal-component CoFeMnTiVZr alloy in electrochemical and gas–solid reactions, RSC Adv. 10 (2020) 24613–24623.